



This is the accepted manuscript made available via CHORUS. The article has been published as:

## Two-dimensional optomechanical crystal resonator in gallium arsenide

Rhys G. Povey, Ming-Han Chou, Gustav Andersson, Christopher R. Conner, Joel Grebel, Yash J. Joshi, Jacob M. Miller, Hong Qiao, Xuntao Wu, Haoxiong Yan, and Andrew N. Cleland

Phys. Rev. Applied **21**, 014015 — Published 10 January 2024

DOI: [10.1103/PhysRevApplied.21.014015](https://doi.org/10.1103/PhysRevApplied.21.014015)

# Two-dimensional optomechanical crystal resonator in gallium arsenide

Rhys G. Povey,<sup>1,2</sup> Ming-Han Chou,<sup>1,2</sup> Gustav Andersson,<sup>2</sup> Christopher R. Conner,<sup>2</sup> Joel Grebel,<sup>2</sup> Yash J. Joshi,<sup>2</sup> Jacob M. Miller,<sup>1,2</sup> Hong Qiao,<sup>2</sup> Xuntao Wu,<sup>2</sup> Haoxiong Yan,<sup>2</sup> and Andrew N. Cleland<sup>2,3,\*</sup>

<sup>1</sup>*Department of Physics, University of Chicago, Chicago IL 60637, USA*

<sup>2</sup>*Pritzker School of Molecular Engineering,  
University of Chicago, Chicago IL 60637, USA*

<sup>3</sup>*Center for Molecular Engineering and Materials Science Division,  
Argonne National Laboratory, Lemont IL 60439, USA*

(Dated: November 21, 2023)

## Abstract

In the field of quantum computation and communication there is a compelling need for quantum-coherent frequency conversion between microwave electronics and infra-red optics. A promising platform for this is an optomechanical crystal resonator that uses simultaneous photonic and phononic crystals to create a co-localized cavity coupling an electromagnetic mode to an acoustic mode, which then via electromechanical interactions can undergo direct transduction to electronics. The majority of work in this area has been on one-dimensional nanobeam resonators which provide strong optomechanical couplings but, due to their geometry, suffer from an inability to dissipate heat produced by the laser pumping required for operation. Recently, a quasi-two-dimensional optomechanical crystal cavity was developed in silicon exhibiting similarly strong coupling with better thermalization, but at a mechanical frequency above optimal qubit operating frequencies. Here we adapt this design to gallium arsenide, a natural thin-film single-crystal piezoelectric that can incorporate electromechanical interactions, obtaining a mechanical resonant mode at  $f_m \approx 4.5$  GHz ideal for superconducting qubits, and demonstrating optomechanical coupling  $g_{\text{om}}/(2\pi) \approx 650$  kHz.

## INTRODUCTION

Spurred on by the promise of quantum computing [1, 2], superconducting qubits [3–9] have become a ubiquitous topic of research and development. These devices, typically operating with microwave electronic frequencies of 4–8 GHz and housed in dilution refrigerators at  $\sim 10$  mK, are excellent candidates for quantum information processing but suffer from an inability to engage in long-range communication due to the lossy environment and large amount of microwave thermal noise at room temperature. To facilitate such connections outside of cryogenic temperatures, a quantum transducer that is able to coherently convert a microwave-electronic quantum state to an infra-red fiber optic signal, ideally in the telecom band of 1530–1565 nm, is desired [10–13]. Of the many approaches being explored for this challenging task, a propitious route is through an optomechanical crystal cavity [14, 15] that emerges by placing a defect in a simultaneous photonic and phononic crystal. This defect site is able to support both a microwave-frequency acoustic resonant mode and an infra-red electromagnetic resonant mode, allowing them to couple to each other. Acoustic modes can

then be directly transduced to electrical signals through a piezoelectric material.

The optomechanical Hamiltonian for an optical resonant mode at  $\omega_o$ , annihilation operator  $\hat{a}$ , and a mechanical resonant mode at  $\omega_m$ , annihilation operator  $\hat{b}$ , is given by

$$\hat{H} = \hbar \omega_o \hat{a}^\dagger \hat{a} + \hbar \omega_m \hat{b}^\dagger \hat{b} + \hbar g_{om} \hat{a}^\dagger \hat{a} (\hat{b}^\dagger + \hat{b}) , \quad (1)$$

where the interaction term, with optomechanical coupling  $g_{om}$ , can be derived by considering an optical Fabry-Pérot mirror attached to a mechanical spring undergoing small oscillations [16, 17]. To obtain an exchange interaction we need to include a strong laser pump at frequency  $\omega_L$ , adding the term  $\hbar L \hat{a}^\dagger e^{-i\omega_L t}$ , where  $L$  is measure of the pump strength. For a strong pump we can expand  $\hat{a}(t) = \hat{a}'(t) + \bar{a} e^{-i\omega_L t}$ , with  $\bar{a} \propto L$ , and linearize for  $\bar{a} \gg \hat{a}'$ . With the laser red-detuned from the optical resonance,  $\omega_L = \omega_o - \omega_m$ , under the rotating wave approximation our interaction term then becomes

$$\hat{H}_{\text{int}} \approx \hbar g_{om} (\bar{a}^* \hat{a}' \hat{b}^\dagger + \bar{a} \hat{a}'^\dagger \hat{b}) , \quad (2)$$

providing a ‘beam-splitter’ swapping interaction that allows infra-red optical excitations to be exchanged with microwave-frequency mechanical excitations. As can be seen in Eq.(2), the optomechanical swapping interaction is enhanced by the average photon number,  $|\bar{a}|^2$ , which is proportional to the laser pump power. Thus to maximize the effective optomechanical coupling, the laser pump should be as strong as possible before detrimental effects, such as heating, set in.

Previous work [18–20] and the majority of attention in optomechanical crystals for transduction has been on one-dimensional nanobeam designs [21–26]. These structures exhibit strong optomechanical coupling,  $g_{om}/(2\pi) \sim 1$  MHz, and high mechanical and optical quality factors but are plagued by poor heat dissipation due to their one-dimensional nature limiting thermal conductivity [27]. Recently, a quasi-two-dimensional optomechanical cavity design consisting of C-shape holes within the waveguide of a snowflake hole crystal lattice was demonstrated in silicon [28]. This device showed improved heat management whilst maintaining good optomechanical coupling and quality factors, however, targeting 194 THz optics, operates at a mechanical frequency near 10 GHz — somewhat above the optimal frequency for popular superconducting qubit archetypes. Here, we adapt the design to gallium arsenide (GaAs), having half the acoustic wave speed of silicon, to produce a

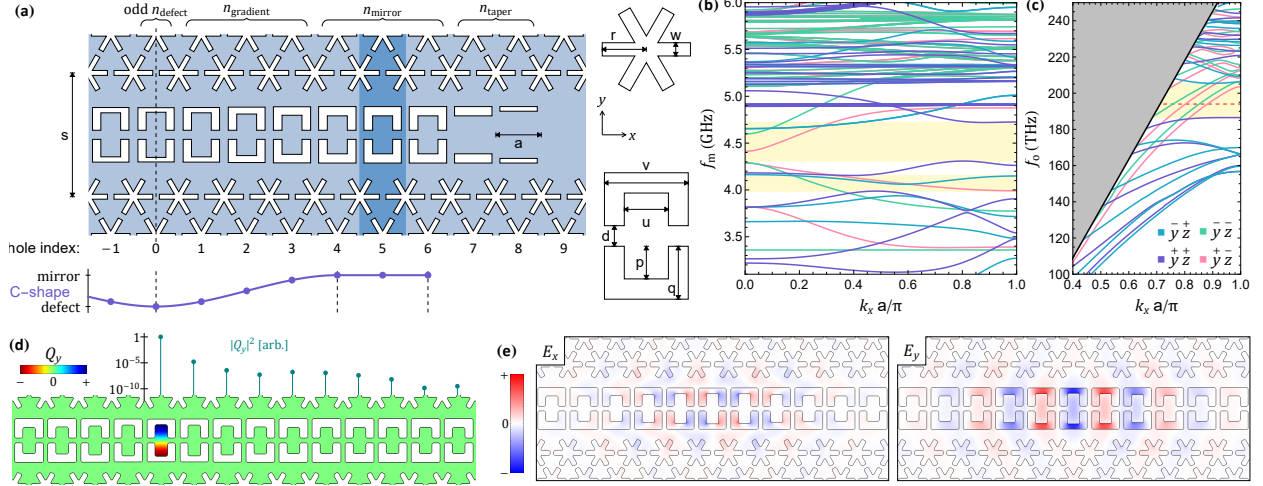


FIG. 1. (a) Layout and geometric parameterization of the optomechanical crystal resonator. The crystal (mirror) unit cell is highlighted. Parameter values in the gradient section between the defect and crystal unit cells are scaled with a  $\text{SmoothStep}_1$  function plotted by the purple line below. (b) Acoustic dispersion relations from finite element model simulations of the mirror unit cell. Band gaps for  $y\text{-}z$  symmetric modes are highlighted by yellow bands. (c) Electromagnetic dispersion relations from finite element model simulations of the mirror unit cell. Band gaps for  $z$  symmetric modes are highlighted in yellow and cover our infra-red frequency of interest, 194 THz, marked with a dashed red line. (d) Simulation of the displacement field,  $Q_y$ , for the paddle breathing mode at 4.63 GHz. Displacements in paddles neighbouring the defect are too small to make out but are plotted above on a log scale. (e) Simulations of the electric field for an electromagnetic resonance at 197 THz. Specific dimensions used for simulations are given in the supplementary materials [29].

two-dimensional optomechanical resonator at a superconducting qubit compatible frequency  $\sim 5$  GHz. Furthermore, the inherent piezoelectricity in gallium arsenide allows for future direct coupling to an electrical circuit.

## DESIGN

To describe the symmetries present in the optomechanical crystal design we use the notation  $\pm x$  to denote a mirror (+) or anti-mirror (−) symmetry through the  $x = 0$  plane, such that

$P_{\vec{x}} \cdot F[P_{\vec{x}} \cdot \vec{r}] = \pm F[\vec{r}]$  for some tensor field  $F$ , where  $P$  is the Householder reflection transform. The main two-dimensional optomechanical crystal is made from snowflake shaped holes in a periodic lattice that exhibits  $\pi/3$  rotational symmetry and mirror symmetries (wallpaper group p6m). This provides a complete acoustic band gap and  $z$  mirror symmetric ( $\overset{+}{z}$ ) electromagnetic band gap [29]. Removing a row of snowflakes, and with additional stretching, creates a waveguide through the two-dimensional optomechanical crystal. C-shape holes along this waveguide in a ‘vertebrae’ pattern form a one-dimensional optomechanical crystal that can be gradually transitioned to create a defect cavity. The layout and parameterization of these holes to form the resonator is given in Fig. 1(a).

C-shape hole dimensions in the gradient region between the mirror and defect are scaled according to the differentiable SmoothStep<sub>1</sub> function, plotted in Fig. 1(a), with definition SmoothStep <sub>$n$</sub>  :  $[0, 1] \rightarrow [0, 1]$  by  $x \mapsto x^{n+1} \sum_{k=0}^n \binom{n+k}{k} \binom{2n+1}{n-k} (-x)^k$ , where  $\binom{n}{k}$  are binomial coefficients. This is the lowest order polynomial between constant zero and one that is  $n$ -differentiable.

Here, we focus on  $n_{\text{defect}} = 1$  single paddle resonances. Although  $n_{\text{defect}} > 1$  resonators provide better optomechanical couplings in simulation, they are prone to fabrication imperfections, splitting the resonance into separate modes. Simulations showed that a +1 nm change in paddle length ( $\mathbf{p}$ ) shifted the individual resonance by  $-17$  MHz.

Starting with C-shape hole parameters used in silicon [28, 30], finite element model simulations [31] were carried out in gallium arsenide and iterated upon to find a set of dimensions that produced the desired band gaps. Dispersion relations for such parameters over a vertebrae unit cell are given in Fig. 1(b,c). The acoustic resonance displacement field must be mirror-symmetric about every geometric mirror plane in order to have non-vanishing optomechanical coupling [29, 32]. For the vertebrae resonator design, this is the paddle breathing mode with mirror symmetries about each cardinal plane through the center ( $\overset{+}{x} \overset{+}{y} \overset{+}{z}$ ) as depicted in Fig. 1(d). By changing the paddle length ( $\mathbf{p}$ ) between the mirror cell and defect cell, we can move the breathing mode from outside the band gap to within.

Eigenvalue simulations of the full vertebrae resonator are shown in Fig. 1(d,e). In order to accommodate future acoustic piezoelectric wave propagation, the waveguide is aligned along

the [110] GaAs crystal axis [32]. With sufficiently large models, the optical mode quality factor was simulated to be  $\sim 26 \times 10^3$ . Simulations for the mechanics, which only include loss through the supports, yield mechanical quality factors in excess of  $10^9$ . Actual mechanical quality factors will be significantly less than this.

The optomechanical coupling, calculated from displacement and electric fields, had a contribution of 358 kHz from moving boundary and 241 kHz from the photo-elastic effect, giving a total  $g_{\text{om}}/(2\pi) = 599$  kHz.

Simulations of heat dissipation comparing the two-dimensional vertebrae design to a one-dimensional nanobeam are available in the supplementary materials [29]. Whilst the heating is highly dependent on the size of the structure, the two-dimensional design offers superior scaling. For the same heating power, a vertebrae optomechanical resonator exhibits a temperature increase an order of magnitude lower than a 40  $\mu\text{m}$  long nanobeam.

## FABRICATION

Devices are fabricated on heterostructure wafers consisting of 250 nm GaAs, on a 1  $\mu\text{m}$   $\text{Al}_{0.9}\text{Ga}_{0.1}\text{As}$  sacrificial layer, on 635  $\mu\text{m}$  bulk (100) GaAs. The relatively low suspension height provided by the sacrificial layer ( $t_{\text{gap}} < \lambda_o$ ) leads to optical fields leaking into the bulk, limiting optical quality factors and grating coupler performance. Simulations of the optical quality factor dependence on suspension height are provided in the supplementary materials [29].

Patterning is performed with electron beam lithography using 14% by weight hydrogen silsesquioxane in methyl isobutyl ketone resist and a chlorine, argon inductively coupled plasma etch. Proximity effect correction is vital when patterning nanometer scale features over hundreds of square microns on a heavy substrate with significant electron back scatter, details of our point spread function used are provided in the supplementary materials [29]. To account for uncertainty in precise slab thickness, produced hole sizes, and simulations, devices are fabricated in series of varying global scale factor, typically in steps of 1%. Parameter dimensions for the pattern used to write the device presented here are listed in the

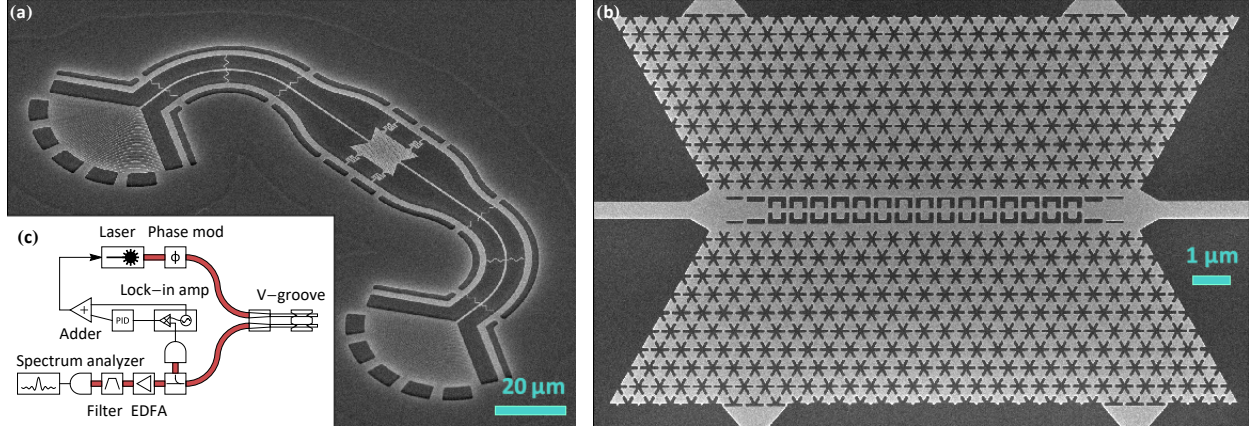


FIG. 2. (a) Scanning electron microscope image, taken at  $45^\circ$ , of a device similar to the one measured here. Two large suspended grating coupler pads deflect light in and out of plane to couple to overhead optical fibers. The optomechanical crystal plate is suspended in the middle with large serpentine tethers to relieve tension during the release process. (b) Magnified image of the optomechanical plate from (a), taken top down, showing the vertebrae resonator. Proximity effect correction during electron beam lithography is essential for uniform snowflakes. (c) Simplified diagram of the optical measurement setup showing only elements discussed in the text. The phase modulator is driven by a microwave frequency signal generator and provides a calibration of power measured by the spectrum analyzer. The V-groove assembly holds fiber optics above the device. A portion of the output signal is used in a dither locking system, utilizing a lock-in amplifier and proportional-integral-derivative (PID) controller, that adjusts the laser output wavelength. The detection chain consists of an erbium doped fiber amplifier (EDFA) followed by a filter to cut out amplified spontaneous emission, and then a microwave-frequency bandwidth photodetector.

supplementary materials [29].

To couple light to the device, two suspended grating coupler pads are used to deflect light in and out of plane to optical fibers positioned above the device. The resonator is then interposed along a connecting suspended waveguide as depicted in Fig. 2(a,b). Although less efficient than tapered-beam edge coupling, this approach allowed up to 100 devices to be fabricated and tested on a single  $1 \text{ cm}^2$  chip.

## MEASUREMENT

Optical measurements are carried out at room temperature using an infra-red fiber optic setup and tunable laser. A simplified diagram including only major elements is shown in Fig. 2(c). To compensate for slow thermal drifts of the optical resonance frequency and overall transmission, a second-harmonic dither locking system is used to track the resonance inflection points. A diagram of the complete setup, and details on the dither locking, are included in the supplementary material [29].

Transmission through the optical resonance is given by

$$|S_{21}(\omega)|^2 = \frac{(\gamma_o^{\text{wg}})^2}{(\omega - \omega_o)^2 + \left(\frac{\gamma_o}{2}\right)^2},$$

with  $\gamma_o = \gamma_o^0 + 2\gamma_o^{\text{wg}}$ , where  $\gamma_o^0$  is intrinsic power loss rate and  $\gamma_o^{\text{wg}}$  is power loss rate to each waveguide port. The loaded quality factor is defined as  $Q_o^L = \omega_o/\gamma_o$ , and the internal quality factor is  $Q_o^0 = \omega_o/\gamma_o^0$ . A captured transmission profile is given in Fig. 3(a).

At room temperature, the mechanical resonance has a thermal population  $\bar{n}_m \approx \frac{k_B T}{\hbar \omega_m} = 1371 \pm 14$ , which through the optomechanical interaction will modulate the optical resonance at the mechanical resonance frequency. Probing the side of the optical resonance, we are sensitive to the resulting power fluctuation using a high bandwidth photodetector, and measuring with a spectrum analyzer can observe the mechanical thermal spectrum.

Conveniently, the transmission factor of this optomechanical spectrum is identical to the transmission factor of a weak phase-modulated signal [33], allowing us to make a calibrated measurement of the optomechanical coupling. At laser frequency  $\omega_L$ , the phase modulated input is  $\exp[-i\omega_L t + iA_\Phi \sin[\omega_\Phi t]]$ . For hot optomechanics,  $\bar{n}_m \gg 1$ , and weak phase modulation,  $A_\Phi \ll 1$ , our power spectral density is, to leading order in  $A_\Phi$ , [29, 32]

$$S_{XX}(\omega > 0) \approx \mathcal{T}(\omega_L; \omega) \left( g_{\text{om}}^2 \frac{\bar{n}_m \gamma_m}{(\omega - \omega_m)^2 + \left(\frac{\gamma_m}{2}\right)^2} + \frac{A_\Phi^2 \omega_\Phi^2}{4} 2\pi \delta(\omega - \omega_\Phi) \right),$$

where  $\gamma_m = \omega_m/Q_m$  is the mechanical mode power loss rate, and  $\mathcal{T}(\omega_L; \omega)$  is a complicated function of the laser frequency and spectrum frequency that includes transmission through the optical cavity and all efficiencies. Using a spectrum analyzer with window function  $w(f_{\text{SA}}, \text{RBW}; f)$ , where  $f_{\text{SA}}$  is the measurement frequency and RBW is the resolution

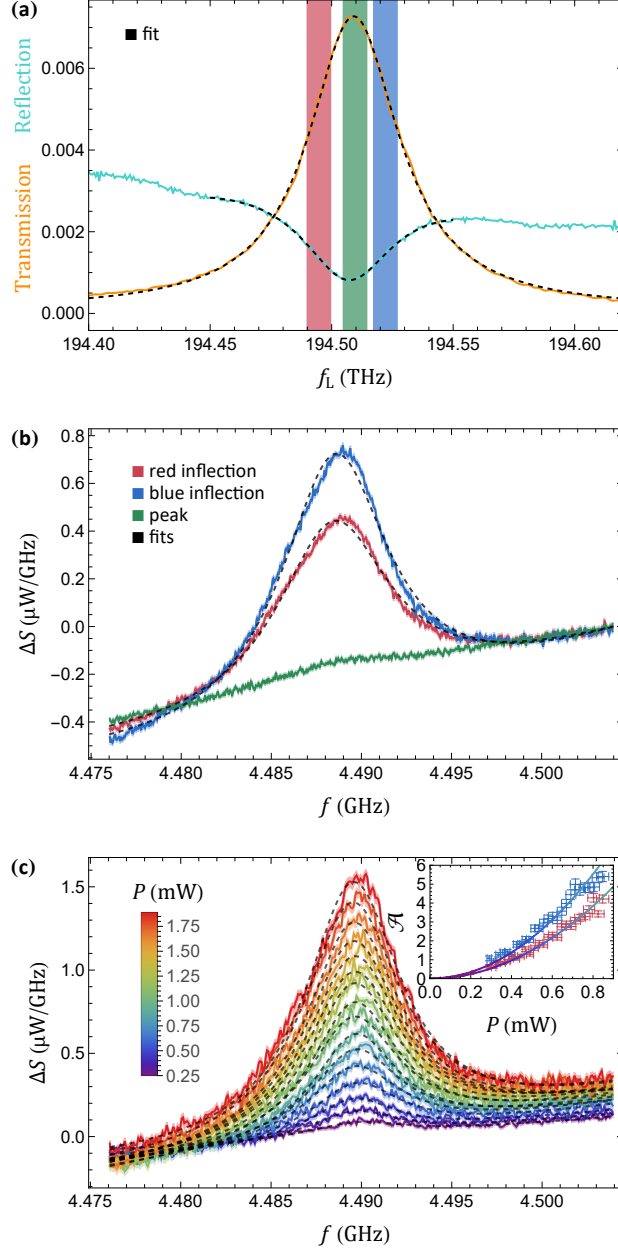


FIG. 3. (a) Full system optical transmission (orange) and reflection (cyan) with colour-coded probing regions covered by the dither lock. Transmission includes waveguide, grating coupler, fiber optic components, and detector efficiencies. (b) Thermal mechanical spectrum imprinted on the optical signal when probed at the optical resonance and inflection points (colour coded accordingly). Each trace is the average of 100 scans with a 100 point moving average, statistical uncertainty of  $\pm 1$  standard deviation is depicted in light shading about the trace. (c) Scans of the thermal mechanical spectrum with different input powers, referenced to the V-groove assembly. Inset shows fit spectrum amplitude  $\mathcal{A}$  as a function of input power over our photodetector's linear operating regime, with  $P^2$  fit curves.

bandwidth, with step size  $\Delta f_{\text{SA}} \ll \text{RBW} \ll \gamma_{\text{m}}/(2\pi)$ , the measured power is

$$P(\omega_{\text{SA}}) = \mathcal{T}(\omega_{\text{L}}; \omega_{\text{SA}}) \left( \text{RBW} 2 g_{\text{om}}^2 \frac{\bar{n}_{\text{m}} \gamma_{\text{m}}}{(\omega_{\text{SA}} - \omega_{\text{m}})^2 + (\frac{\gamma_{\text{m}}}{2})^2} + \frac{A_{\Phi}^2 \omega_{\Phi}^2}{2} w(\omega_{\text{SA}}, \text{RBW}; \omega_{\Phi}) + \text{bg} \right).$$

A broad background, denoted by  $\text{bg}$ , can be removed with a low-order polynomial fit. If  $\omega_{\Phi} \approx \omega_{\text{m}}$ , then  $\mathcal{T}(\omega_{\text{L}}; \omega_{\text{SA}})$  is approximately constant. Fitting the window function over the phase modulated signal (with known amplitude  $A_{\Phi}$ ) allows us to determine  $\mathcal{T}$ , then fitting the thermal spectrum gives us  $g_{\text{om}}$ . For fast scans with no averaging, there is a dither imprint that can be included in the fit or ignored.

In practice, a fit over the thermal spectrum gives us  $\omega_{\text{m}}$ ,  $\gamma_{\text{m}}$ , and the parameter  $\mathcal{A} = 2\mathcal{T} g_{\text{om}}^2 \bar{n}_{\text{m}} \gamma_{\text{m}}$ , whilst a window fit over the phase modulation signal gives us  $P_{f_{\Phi}} = \mathcal{T} A_{\Phi}^2 \omega_{\Phi}^2 / 2$ , such that

$$g_{\text{om}} = \frac{\omega_{\Phi} A_{\Phi}}{\sqrt{k_{\text{B}} T / \hbar}} \sqrt{\frac{\omega_{\text{m}} \mathcal{A}}{4 \gamma_{\text{m}} P_{f_{\Phi}}}}.$$

Spectrum scans are fit individually with each producing  $\sqrt{\frac{\omega_{\text{m}} \mathcal{A}}{4 \gamma_{\text{m}} P_{f_{\Phi}}}}$ , and these are combined together to give a factor that contains all the statistical uncertainty. Temperature,  $T$ , and phase modulation strength,  $A_{\Phi}$ , are included with systematic uncertainties.

The inset of Fig. 3(a) shows the optical resonance transmission and reflection, fits give  $f_{\text{o}} = 194.5$  THz with loaded quality factor  $Q_{\text{o}}^{\text{L}} \approx 4300$  and internal quality factor  $Q_{\text{o}}^{\text{0}} \approx 8600$ . Using a first-harmonic dither lock to the resonance peak (shown in green) there is no optomechanical spectrum visible, as expected. With a second-harmonic dither lock to either of the resonance inflection points (blue and red), the thermal optomechanical spectrum can be seen at  $f_{\text{m}} = 4.488$  GHz with quality factor  $Q_{\text{m}} \approx 600$ . Fig. 3(b) shows the optomechanical spectrum averaged over 100 scans.

Optomechanical couplings are calculated for each individual scan by fitting the thermal spectrum and phase modulate signal. The weighted mean from 100 scans at both the blue and red inflection points yielded  $g_{\text{om}}/(2\pi) = (649 \pm 8)$  kHz.

Scans made at varied laser probe powers are shown in Fig. 3(c). The current output of our photodetector is proportional to the laser power received, giving the power of the measured signal proportional to the square of laser power. This scaling of the thermal power spectrum amplitude,  $\mathcal{A}$ , is shown in the inset.

## DISCUSSION

We have demonstrated a quasi-two-dimensional optomechanical resonator in gallium arsenide, using the vertebrae design, with an optical resonance in the infra-red C band and mechanical resonance at  $\sim 4.5$  GHz compatible with transmon superconducting qubits. The optomechanical coupling of  $\sim 650$  kHz is slightly less than the best demonstrated couplings of  $\sim 1$  MHz [21, 28], however there is significant room for improvement in design parameter optimization, fabrication, and cryogenic operation. Transitioning to edge coupling in reflection will open up the other side of the vertebrae resonator to electromechanical coupling.

The low suspension height of about  $1\ \mu\text{m}$  impacts the optical performance, as evidenced by certain devices that were warped out-of-plane and demonstrated higher optical quality factors. Unfortunately this likely has a negative impact on the mechanical performance. High aluminum content in the sacrificial layer, in addition to hastening the release process, also has a tendency to leave behind difficult-to-remove compounds. Switching to a  $3\ \mu\text{m}$   $\text{Al}_{0.7}\text{Ga}_{0.3}\text{As}$  sacrificial layer should provide easily obtainable gains [21]. The corresponding gentler release would further allow removal of the flexible tethers supporting the optomechanical crystal to realize more thermal contact to the larger chip.

Pattern fabrication precision for two-dimensional devices is challenging compared to one-dimensional devices, particularly with the high atomic weight substrate that exhibits strong electron beam proximity effects. Minor imperfections in the optomechanical crystal are inherently more common and degrade both optical and mechanical quality factors.

## ACKNOWLEDGEMENTS

The authors would like to thank Peter Duda for helpful discussions. This work was supported by the LPS/ARO award W911NF-23-1-0077, NSF QLCI for HQAN (award 2016136), by the Air Force Office of Scientific Research, and in part based on work supported by the U.S. Department of Energy Office of Science National Quantum Information Science Research Centers, and by UChicago's MRSEC (NSF award DMR-2011854). This work made use of

the Pritzker Nanofabrication Facility, part of the Pritzker School of Molecular Engineering at the University of Chicago, which receives support from Soft and Hybrid Nanotechnology Experimental (SHyNE) Resource (NSF ECCS-2025633), a node of the National Science Foundation's National Nanotechnology Coordinated Infrastructure.

---

\* anc@uchicago.edu

- [1] A. Steane, Quantum computing, *Reports on Progress in Physics* **61**, 117 (1998).
- [2] J. Preskill, Quantum computing in the NISQ era and beyond, *Quantum* **2**, 79 (2018).
- [3] Y. Nakamura, Y. A. Pashkin, and J. S. Tsai, Coherent control of macroscopic quantum states in a single-Cooper-pair box, *Nature* **398**, 786 (1999).
- [4] J. Q. You and F. Nori, Quantum information processing with superconducting qubits in a microwave field, *Physical Review B* **68**, 064509 (2003).
- [5] A. Blais, R.-S. Huang, A. Wallraff, S. M. Girvin, and R. J. Schoelkopf, Cavity quantum electrodynamics for superconducting electrical circuits: An architecture for quantum computation, *Physical Review A* **69**, 062320 (2004).
- [6] L. Frunzio, A. Wallraff, D. Schuster, J. Majer, and R. Schoelkopf, Fabrication and characterization of superconducting circuit QED devices for quantum computation, *IEEE Transactions on Applied Superconductivity* **15**, 860 (2005).
- [7] G. Wendin, Quantum information processing with superconducting circuits: a review, *Reports on Progress in Physics* **80**, 106001 (2017).
- [8] S. Kwon, A. Tomonaga, G. L. Bhai, S. J. Devitt, and J.-S. Tsai, Gate-based superconducting quantum computing, *Journal of Applied Physics* **129**, 041102 (2021), arxiv:2009.08021 [quant-ph].
- [9] Y. Y. Gao, M. A. Rol, S. Touzard, and C. Wang, Practical guide for building superconducting quantum devices, *PRX Quantum* **2**, 040202 (2021), arxiv:2106.06173 [quant-ph].
- [10] N. J. Lambert, A. Rueda, F. Sedlmeir, and H. G. L. Schwefel, Coherent conversion between microwave and optical photons: An overview of physical implementations, *Advanced Quantum Technologies* **3**, 1900077 (2020).
- [11] N. Lauk, N. Sinclair, S. Barzanjeh, J. P. Covey, M. Saffman, M. Spiropulu, and C. Simon, Perspectives on quantum transduction, *Quantum Science and Technology* **5**, 020501 (2020).

- [12] Y. Chu and S. Gröblacher, A perspective on hybrid quantum opto- and electromechanical systems, *Applied Physics Letters* **117**, 150503 (2020), arxiv:2007.03360 [quant-ph].
- [13] G. Moody, V. J. Sorger, D. J. Blumenthal, P. W. Juodawlkis, W. Loh, C. Sorace-Agaskar, A. E. Jones, K. C. Balram, J. C. F. Matthews, A. Laing, M. Davanco, L. Chang, J. E. Bowers, N. Quack, C. Galland, I. Aharonovich, M. A. Wolff, C. Schuck, N. Sinclair, M. Lončar, T. Komljenovic, D. Weld, S. Mookherjea, S. Buckley, M. Radulaski, S. Reitzenstein, B. Pingault, B. Machielse, D. Mukhopadhyay, A. Akimov, A. Zheltikov, G. S. Agarwal, K. Srinivasan, J. Lu, H. X. Tang, W. Jiang, T. P. McKenna, A. H. Safavi-Naeini, S. Steinhauer, A. W. Elshaari, V. Zwiller, P. S. Davids, N. Martinez, M. Gehl, J. Chiaverini, K. K. Mehta, J. Romero, N. B. Lingaraju, A. M. Weiner, D. Peace, R. Cernansky, M. Lobino, E. Diamanti, L. T. Vidarte, and R. M. Camacho, 2022 roadmap on integrated quantum photonics, *Journal of Physics: Photonics* **4**, 012501 (2022).
- [14] M. Eichenfield, J. Chan, R. M. Camacho, K. J. Vahala, and O. Painter, Optomechanical crystals, *Nature* **462**, 78 (2009).
- [15] A. H. Safavi-Naeini and O. Painter, Design of optomechanical cavities and waveguides on a simultaneous bandgap phononic-photon crystal slab, *Optics Express* **18**, 14926 (2010).
- [16] M. Aspelmeyer, T. J. Kippenberg, and F. Marquardt, Cavity optomechanics, *Reviews of Modern Physics* **86**, 1391 (2014).
- [17] M. Aspelmeyer, T. J. Kippenberg, and F. Marquardt, eds., *Cavity optomechanics*, Quantum Science and Technology (Springer Berlin Heidelberg, 2014).
- [18] J. Bochmann, A. Vainsencher, D. D. Awschalom, and A. N. Cleland, Nanomechanical coupling between microwave and optical photons, *Nature Physics* **9**, 712 (2013).
- [19] A. Vainsencher, K. J. Satzinger, G. A. Pears, and A. N. Cleland, Bi-directional conversion between microwave and optical frequencies in a piezoelectric optomechanical device, *Applied Physics Letters* **109**, 033107 (2016).
- [20] G. A. Pears, M.-H. Chou, A. Bienfait, H.-S. Chang, C. R. Conner, É. Dumur, J. Grebel, R. G. Povey, E. Şahin, K. J. Satzinger, Y. P. Zhong, and A. N. Cleland, Continuous and time-domain coherent signal conversion between optical and microwave frequencies, *Physical Review Applied* **14**, 061001(R) (2020).
- [21] M. Forsch, R. Stockill, A. Wallucks, I. Marinković, C. Gärtner, R. A. Norte, F. van Otten, A. Fiore, K. Srinivasan, and S. Gröblacher, Microwave-to-optics conversion using a mechanical

- oscillator in its quantum ground state, *Nature Physics* **16**, 69 (2019).
- [22] M. Mirhosseini, A. Sipahigil, M. Kalaei, and O. Painter, Superconducting qubit to optical photon transduction, *Nature* **588**, 599 (2020), arxiv:2004.04838 [quant-ph].
- [23] W. Jiang, C. J. Sarabalis, Y. D. Dahmani, R. N. Patel, F. M. Mayor, T. P. McKenna, R. V. Laer, and A. H. Safavi-Naeini, Efficient bidirectional piezo-optomechanical transduction between microwave and optical frequency, *Nature Communications* **11**, 1166 (2020).
- [24] G. Arnold, M. Wulf, S. Barzanjeh, E. S. Redchenko, A. Rueda, W. J. Hease, F. Hassani, and J. M. Fink, Converting microwave and telecom photons with a silicon photonic nanomechanical interface, *Nature Communications* **11**, 4460 (2020), arxiv:2002.11628 [quant-ph].
- [25] R. Stockill, M. Forsch, F. Hijazi, G. Beaudoin, K. Pantzas, I. Sagnes, R. Braive, and S. Gröblacher, Ultra-low-noise microwave to optics conversion in gallium phosphide, *Nature Communications* **13**, 6583 (2022), arxiv:2107.04433 [quant-ph].
- [26] S. Hönl, Y. Popoff, D. Caimi, A. Beccari, T. J. Kippenberg, and P. Seidler, Microwave-to-optical conversion with a gallium phosphide photonic crystal cavity, *Nature Communications* **13**, 2065 (2022), arxiv:2105.13242 [physics.optics].
- [27] G. S. MacCabe, H. Ren, J. Luo, J. D. Cohen, H. Zhou, A. Sipahigil, M. Mirhosseini, and O. Painter, Nano-acoustic resonator with ultralong phonon lifetime, *Science* **370**, 840 (2020), arxiv:1901.04129 [cond-mat.mes-hall].
- [28] H. Ren, M. H. Matheny, G. S. MacCabe, J. Luo, H. Pfeifer, M. Mirhosseini, and O. Painter, Two-dimensional optomechanical crystal cavity with high quantum cooperativity, *Nature Communications* **11**, 3373 (2020).
- [29] See Supplemental Material at [URL will be inserted by publisher].
- [30] C. M. Kersul, R. Benevides, F. Moraes, G. H. M. de Aguiar, A. Wallucks, S. Gröblacher, G. S. Wiederhecker, and T. P. M. Alegre, Silicon anisotropy in a bi-dimensional optomechanical cavity, *APL Photonics* **8**, 056112 (2023), arXiv:2211.10573 [quant-ph].
- [31] COMSOL AB, COMSOL Multiphysics®.
- [32] R. G. Povey, *Two-Dimensional Optomechanical Resonators in Gallium Arsenide*, Ph.D. thesis, University of Chicago (2023).
- [33] M. L. Gorodetsky, A. Schliesser, G. Anetsberger, S. Deleglise, and T. J. Kippenberg, Determination of the vacuum optomechanical coupling rate using frequency noise calibration, *Optics Express* **18**, 23236 (2010).